27. P. Thomas and P. J. Gierasch, *Science* **230**, 175 (1985).
28. J. E. Tillman, L. Landberg, S. E. Larsen, *J. Atmos. Sci.* **51**, 1709 (1994).
29. A. O. Nier and M. B. McElroy, *J. Geophys. Res.* **82**, 4341 (1977).
30. The ASI/MET science team would like to acknowledge the enthusiasm, dedication, and hard work of the engineering teams who built the accelerometer and MET instruments; the Pathfinder spacecraft en-

Results from the Mars Pathfinder Camera

P. H. Smith*, J. F. Bell III, N. T. Bridges, D. T. Britt, L. Gaddis, R. Greeley, H. U. Keller, K. E. Herkenhoff, R. Jaumann, J. R. Johnson, R. L. Kirk, M. Lemmon, J. N. Maki, M. C. Malin, S. L. Murchie, J. Oberst, T. J. Parker, R. J. Reid, R. Sablotny, L. A. Soderblom, C. Stoker, R. Sullivan, N. Thomas, M. G. Tomasko, W. Ward, E. Wegryn

Images of the martian surface returned by the Imager for Mars Pathfinder (IMP) show a complex surface of ridges and troughs covered by rocks that have been transported and modified by fluvial, aeolian, and impact processes. Analysis of the spectral signatures in the scene (at 440- to 1000-nanometer wavelength) reveal three types of rock and four classes of soil. Upward-looking IMP images of the predawn sky show thin, bluish clouds that probably represent water ice forming on local atmospheric haze (opacity ~0.5). Haze particles are about 1 micrometer in radius and the water vapor column abundance is about 10 precipitable micrometers.

P. H. Smith, D. T. Britt, M. Lemmon, R. J. Reid, M. G. Tomasko, E. Wegryn, Lunar and Planetary Laboratory, University of Arizona, Tucson, AZ 85721, USA.
J. F. Bell III and R. Sullivan, Cornell University, Ithaca , NY 14853, USA.
N. T. Bridges, K. E. Herkenhoff, J. N. Maki, T. J. Parker, Jet Propulsion Laboratory, California Institute of Technology, Pasadena, CA 91109, USA.
L. Gaddis, J. R. Johnson, R. L. Kirk, L. A. Soderblom, W. Ward, U.S. Geological Survey, Flagstaff, AZ 86001, USA.
R. Greeley, Arizona State University, Tempe, AZ 85287, USA.
H. U. Keller, R. Sablotny, N. Thomas, Max Planck Institute for Aeronomy, Kathenburg–Lindau, Germany.
R. Jaumann and J. Oberst, DLR, Berlin, Germany.
M. C. Malin, Malin Space Science Systems, San Diego, CA 92191, USA.
S. L. Murchie, Applied Physics Laboratory, Johns Hopkins University, Baltimore, MD 21218, USA.
C. Stoker, NASA Ames Research Center, Moffett Field, CA 94035, USA.

*To whom correspondence should be addressed. E-mail: psmith@lpl.arizona.edu

After Mars Pathfinder's landing on 4 July 1997, the Imager for Mars Pathfinder (IMP) (*1*) returned the first pictures of Mars from the surface since the Viking missions 21 years before. The panoramic views (Plate 1A) show a terrain littered with boulders stretching to a horizon graced by two hills (the "Twin Peaks"), the southern one conical with a vertical stripe, the northern one broader and banded with possible terraces. But stereoscopic views (Plate 1B) later revealed that the terrain between the lander and the Twin Peaks was a series of shallow gullies, some filled with fines material. This ridge and trough structure appears to be a remnant of the catastrophic floods that came through this area more than 2 billion years ago from Tiu Vallis, southwest to northwest trend, and from Ares Vallis, south-southeast to north-northwest trend.

Here, along with (*2*), we present results on a range of topics from the geomorphology and mineralogy of the site to the atmospheric properties and astronomical observations. During the first 30 days of operation, the IMP returned 9669 images from the surface of Mars; many of these are subframes taken of the sun, various targets on the lander, or multispectral spots on selected rocks and soil. The large panoramas (Plate 1) and their characteristics are listed in Table 1.

Overview of the Pathfinder landing site. The Pathfinder landing site, at the mouth of the Ares and Tiu flood channels, was selected as an area likely to have a diversity of rock types (*3*). As observed from orbit, the principal elements of the geology of the area include (i) relatively smooth plains, (ii) scattered hills that appear to be remnants of a former, eroded surface, (iii) impact crater rims and other ejecta deposits, and (iv) streamlined tails behind topographically prominent features. The southern Chryse plains are pitted by primary and secondary impact craters that indicate a late Hesperian to early Amazonian age. Mem-

bers of two secondary impact crater clusters lie within 10 km of the lander, toward the southeast and north-northeast. Faint lineaments, trending southwest-northeast, are seen throughout the region following the same trend as the terraced remnants of channels and large tails that occur down slope of the hills. Divergence of these lineaments beyond the mouths of channels reinforces the impression that they are streamlines.

Postflood, geomorphic processes have been relatively benign neither physical nor chemical weathering has led to substantial deterioration of boulders. Derivative debris surrounding rocks is minimal and where debris is collected around boulders, it appears as thin lag deposits atop bright fines, and therefore is interpreted to be aeolian in derivation. Some rocks show indisputable evidence of abrasion, which attests to a flux of saltating particles through the area at some point, although none of the rocks shows the extreme abrasion expected for two or more billion years of exposure to sand blasting at martian wind speeds. At the Viking landing sites, where evidence for abrasion was limited and for sand was disputed, it was suggested that the rocks could have been buried or that windblown particles were incapable of abrasion. Clear evidence of rock abrasion at the Pathfinder site suggests, and may require, sand-transporting winds.

Sight lines to large distant knobs are useful for locating the landing site on the Viking orbiter images; the landing site is about 3 km north-northwest of a 1.5 km diameter impact crater and 1 km east of two hills less than 50 m tall (*3*). Viking orbiter images suggest that a subtle, kilometer-wide asymmetrical rise lies immediately west of the landing site, and that this rise has a short, steep west-northwestern slope and a gentler east-southeastern slope. The twin hills are located along the crest at the western (presumably upstream) end of this ridge. The lander is located on a south-facing slope near the northernmost extension of the rise, close to the point where the relief becomes indistinguishable from the flatter plains. The portion of the rise that extends north of the lander hides all but the summit of a 100 m hill located about 2 km north of the lander.

The Pathfinder site is more rugged than either of the Viking landing sites (*4*) and has a pronounced ridge-and-trough texture (Plates 2 and 4). Over distances of 50 to 100 m, these ridges and troughs have amplitudes as high as 5 m, and are irregularly spaced but commonly 15 to 25 m crest-to-crest. Southwest-northeast and south-north trends comparable with the large-scale Tiu and Ares flow directions are modestly ex-

pressed. A weaker southeast-northwest trend which follow the local topography is also apparent. The lander came to rest in a slight, asymmetrical swale that is open to the south and east; a small ridge of boulders, the "Rock Garden," defines the western rim of this depression.

Rocks and coarse debris. Rocks ranging in size from a few centimeters to as large as 7 m are seen in all directions from the lander, although their distribution is far from uniform. The eastern half of the scene is deficient in rocks relative to the other half (3). For statistically large samples (>20 m^2), the percentage of surface occupied by rocks greater than 2 to 3 cm in size varies azimuthally by over a factor of three—at its maximum, the density approaches 30%, but averages 16% (Plate 8). The rock size variation resembles that seen at the Viking sites; at large diameters, the Pathfinder distribution falls between the Viking 1 lander (VL-1) and VL-2 populations (Plate 9). The Pathfinder site has many more cobbles and pebbles than the Viking sites. Small swales appear filled with fine debris and covered with a lag of gravel. These particles may be lithic or monomineralic fragments, or pieces of indurated soil. There is no evidence for specific minerals.

Boulder and cobble populations differ in several ways. The size to frequency relationship is characterized by a convex-upward curve for smaller particles, but larger boulders deviate substantially from this shape. Larger rocks are typically rounded but some are tabular (Plate 1). Smaller cobbles and pebbles are generally equidimensional, platy, and subangular. Most rocks are not in physical contact with one another, particularly for diameters less than 15 cm. However, in the rocky terrain west of the lander, large rocks are commonly in contact with each other and in places imbrication in a south to north orientation is suggested (Plate 1).

Red deposits on the upper surfaces of many rocks at the landing site are inferred to be dust (5) settled from suspension in the atmosphere. Dust also accumulated on lander and rover solar panels at a rate of 0.3% area coverage per day in the first few

weeks of operation. Small magnets on the lander attracted dust during the nominal mission, verifying the Viking observations of magnetic dust grains in the atmosphere and soil (2). This deposition could be related to the dust cloud observed by the Hubble Space Telescope (6) during this same period.

At least three dune forms are observed, two linear deposits (Mermaid and Roadrunner) and one with a barchanoid outline (Jenkins). All have smooth surfaces that blend as feather edges with the surrounding terrain from crestlike summits. The two linear features are 2.0 m and 50 m long; the barchanoid feature is ~3 m measured across the "horns." The dune forms are estimated to be less than 15 cm high. The majority of these Pathfinder features have higher albedo than the dunes seen from orbit; the interpretation is that the sediments rocks composing the Roadrunner and perhaps Jenkins dune forms are "light" in color, and therefore not basaltic sand but perhaps felsic particulates.

Soil forms a general background surface of bright and dark deposits in which most of the rocks are set. In some places, the soil has a ripple-like pattern in which the troughs are dark and the crests are bright. The wavelengths of this pattern range from 2 to 4 cm. On Earth, such dune forms and the ripple-like patterns develop mainly from saltating sand (7). However, the ripple-like patterns lack the repetitive spacing, coherent wave fronts, modest height-to-length ratio, and asymmetric relief of terrestrial sand ripples.

Wind sock results. Three IMP windsocks were deployed with the atmospheric structure investigation/meterology (ASI/MET) mast on sol 1 (at 58, 82, and 112 cm), and a regular program of daily windsock imaging was established on sol 13. Wind speed and azimuth were calculated from the three-dimensional appearance of each windsock in each image, the spacecraft tilt and camera attitude parameters, and the ASI/MET temperature and pressure data (for atmospheric density).

Winds were light during the primary mission (sols 13 to 35), usually less than 8 m/s. Wind conditions around 0850 and

1630 LST were typically calmer, less than 5 m/s. Stronger winds, generally from the west, were common from late morning to early afternoon. A peak wind speed of 12 m/s was measured from the WSW at 1130 LST on sol 32. The strongest winds measured so far are still relatively light and are not from azimuths parallel to wind tails and other surface features indicative of much stronger winds and aeolian activity.

Aeolian processes. Several rocks in the vicinity of the lander display features that are most likely the result of aeolian action. Small rocks southeast of the lander have scallop-shaped depressions ("flutes") and narrow longitudinal grooves reminiscent of terrestrial ventifacts. Such evidence of wind action was absent at the Viking sites (8).

Wind streaks are surface albedo patterns that change their size, shape, and position with time and represent the primary wind directions at the time of their formation (9). To assess the processes reflected by the fine material at the Pathfinder site, we measured the orientations of aeolian features using a virtual reality model (Plate 3 (10)). Down-tail azimuths of the wind tails range from 179° to 251°, with an average of 217°. The axes of dune forms and ripple-like patterns are oriented northwest-southeast, about orthogonal to the wind tail orientations. As photographed by the Viking Orbiters, the Ares-Tiu area shows prominent bright wind streaks, oriented at 213°.

A Mars general circulation model (GCM) enables the near-surface wind patterns to be predicted as a function of martian season and location on Mars (11).
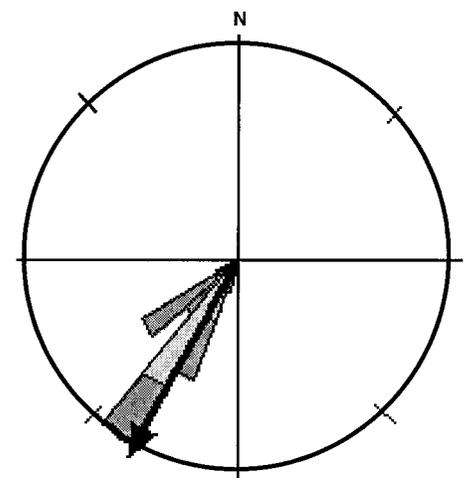

Fig. 1. Rose diagram showing orientations of wind tails at the Pathfinder site (dark gray), bright wind streaks seen on Viking Orbiter images of the area 60 to 90 km northeast of the site (light gray), and Mars General Circulation Model results (black arrow) for winds predicted at the site in northern winter.

Table 1. IMP panorama summary. The types of panoramas that were returned during the mission.

Name	Sol obtained	Mast	Comment
Airbag assessment	1	Stowed	Compression 80:1
Mission success	1	Stowed	120° true color, high compression, full pan red stereo (6:1)
Insurance	2	Stowed	Six filters, low compression
Monster	3	Deployed	True color middle 2 tiers, red stereo tiera (6:1)
Gallery	8–10	Deployed	True color, 6:1
Super	13–84	Deployed	All 15 filters, 2:1

GCM results for the landing site show that the strongest winds should occur in the winter and are oriented with a downwind azimuth of 209°. The correlation of all three patterns (Fig. 1) is similar and leads to the conclusion that the wind tails, dune forms, and ripple-like patterns are aeolian in origin and result from the effects of prevailing winter winds.

Wind tails at the Pathfinder site (Plate 7A) range in length from less than a cm to about 40 cm, and have a sculpted appearance similar to those seen at VL-1 (4). They are widest and highest at the end closest to the rock with which they are associated, and taper to a point at the other end. Deposits similar to wind tails are also seen in association with some rocks, but these deposits lack the tapered form and are referred to as drifts. The maximum height above the surrounding surface of eight wind tails was ~13 cm.

Many of the rocks in the Rock Garden show albedo differences and are darker near their tops (Fig. 2). The division between the two albedo regions was at 5 to 7 cm above the surface for the five rocks measured. This line is interpreted to represent the surface of a former soil level that has been deflated, or stripped, to form the current surface; these albedo differences may represent different exposure ages.

Fluvial and impact processes. Several aspects of the Pathfinder landing site support the notion that the location was affected by a large flood (3). Among these factors are the size, shape, and distribution of coarse materials, the pattern of decameter-scale relief, and relationships seen on the twin hills west of the site. Comparison of the observed size relationships with those seen in Iceland (12), especially for the largest rocks, and the sharp-edged tabular shapes, and the burial relationships and absence of exposed gravel deposits, suggests a waning phase, late-stage deposition of locally derived debris that has not traveled great distances.

Many of the smaller rocks on the surface may be ejecta from nearby impact craters. Impact crater ejecta models show that ejecta thickness and volumetric size/frequency decreases radially as an inverse 3.5 power law, suggesting that at the Pathfinder site over 0.5 m of material could have been discontinuously deposited from the large crater to the south (13). At 1.2 crater diameters away, most of this ejecta should be 5 to 20 cm across.

Boulder trains seen in distant views of the twin hills resemble landforms found in the lee of obstacles in large terrestrial floods. The ridge-and-valley topography is generally consistent with fluvial landforms developed in and comprised of mobile sedimentary material. However, the topography is not diagnostic; glacial and periglacial processes can create similar relief and it is possible that the relief mimics bedrock topography veiled by a thin mantle of debris.

Empirical relationships derived from studies of terrestrial flood deposits (14) are used to infer some of the attributes of the floods that affected the landing site. For example, the size of largest materials moved by a flood as bed load is related to the depth of the flood, the velocity of the flow, and the topographic slope (15). The mean diameter of the five largest boulders within 75 m of the landing site is determined to be 1.8 m. Earth-based radar and orbital photogrammetric analyses suggest that the gradient in the vicinity of the Pathfinder landing site is between 1 km in 400 km and 1 km in 1000 km (16). Using these values with the empirical relationships and accounting for the difference in gravitational acceleration, the flow velocity is computed to have been about 8 m/s and the flow depth 10 to 20 m, not including wake splash. This is about 1/3 to 2/3 the height of the northern twin peak and 1/4 to 1/2 the height of the southern peak, and is consistent with the slope morphology and position of boulders on these peaks. Velocities of 10 to 15 m/s are typical for step-backwater calculations for confined floods in Ares and Kasei Valles (17). The flow depths determined here are a factor of 20 to 50 times less than those used in the step-backwater calculations, but they are consistent with values calculated for large floods in Iceland and Washington state (18).

Discharge cannot be computed without good cross sections of the channel, but the fluid properties of water (even debris-laden water) and the generally small size of the bed load (generally smaller than a meter) suggests that discharges were between 10^6 and 10^7 m³/s in the immediate vicinity of the lander. These values are one to two orders of magnitude smaller than previous estimates (17), but are not surprising considering the great difference in scale at which the determinations were made.

IMP spectral data and calibration. Target rocks and soils were imaged as 64 by 64 pixel subframes in all 15 geological spectral filters at 12 wavelengths. For spectral calibration the IMP radiometric calibration targets were imaged concurrently in the same filters (1).

The illumination onto the surface and the radiometric targets is a combination of

Fig. 2. IMP image of the Rock Garden showing horizontal line (marked by white arrows) on some rocks inferred to represent former soil horizon.

Table 2. Spectral unit summary; R/B, red/blue.

Type name	Type location	Spectral characteristics			Interpretation
		I/F (@ 750 nm)	R/B ratio	Kink	
Bright soil	Near cradle and Yogi	26 to 35%	3.69 to 3.76	0.3 to 0.31	Similar to global dust
Dark soil	Photometry Flats, Mermaid	16 to 19%	2.85 to 3.0	0.2 to 1.16	Local weathering product
Lamb-like soil	Near Lamb	23%	3.46	0.3	Mixture of dust and local material
Disturbed soil	Rover Tracks	22 to 25%	3.11 to 3.76	0.15 to 0.54	Soil compaction changes scattering
Dark rock	Barnacle Bill, Bamm-Bamm	12 to 14%	2.06 to 2.11	0.09	Fresh basalt or basaltic andesite
Bright rock	Broken Wall, Wedge	19 to 24%	2.8	0.18	Weathered basalt or basaltic andesite
Pink rock	Scooby Doo, Baker's Bench	33 to 36%	4.0 to 4.2	0.28 to 0.33	Chemically cemented drift

the direct sun and the diffuse sky flux. The sky contribution depends on the dust loading in the atmosphere. During the 30-day primary mission, the vertical optical depth (τ) was calculated from direct solar observations as ~0.5. This agrees with the Viking lander data for this season (*19*). For example, in the 670-nm (red) filter at local solar noon the sky brightness is ~40% of the downward flux, while at 4 PM LST this contribution increases to ~50% (*20*).

The sky color is not neutral, but is reddened by the global dust; the greatest signal is from 650 to 1000 nm (*21*). This effect reddens surface materials to various degrees depending on the orientation of rock faces. The IMP radiometric calibration targets are designed to remove the coloration of the sky on rocks and soil when they are parallel to the target. The soils generally fulfill this condition while the rocks have steeply sloped sides and their spectra must be viewed with caution.

Spectral image data show evidence for at least four soil types at the landing site (Table 2) (*22*). The two most common soil types are labeled "bright soil" and "dark soil" (Fig. 3). Bright and dark soils are end-members, and soils have been detected that span the reflectance range between these two units. Bright soil material is typically found in shallow aeolian deposits near and around rocks and as thin ground cover in many areas of the Pathfinder site. The type areas are near the rocks Cradle and Yogi (Plate 6). Reflectance spectra of bright soil are red and bright, peaking in relative reflectance(*23*) at 750 nm with values of 35% for Cradle soil and 28% for Yogi soil. This type has a high red/blue ratio and a moderate kink parameter (*24*), indicative of an oxidized ferric-rich soil (*25*) (Table 2). Bright soil spectra lack the weak 800 to 900 nm absorption found in the planet-wide dust (*26, 27*), yet a global dust origin for bright soil is consistent with the wide distribution of this material around the Pathfinder site. The action of the rover wheels exposed other materials under the disturbed soil indicating a shallow depth. For comparison telescopic spectra of the bright and dark martian regions are plotted as well as a palagonitic soil often used as a martian analog (*26, 27*).

The type areas for the dark soil unit are Photometry Flats and Mermaid. This material occurs in dune forms, patches between rocks and in small aeolian bedforms. Dark soil is the lowest reflectivity soil at the site (for example, 750-nm reflectance at Photometry Flats is 16%). The red/blue ratio and the kink are in the moderate range (Table 2). The overall spectrum indicates that this unit is less oxidized than the

bright soil material and is intermediate between the global dust-like bright soil and the spectra of most rocks in the area. One interpretation of these data is that the dark soil is an intermediate weathering product that retains some of the relatively unstable mafic silicates from the parent basalts and has not completed its ferric oxidation process. An alternative is that the dark soil may have a larger particle size than the bright soil, which leads this material to be preferentially sorted away from the bright soil.

The other two soil units are localized. The Lamb-like soil unit occurs primarily near the rock Lamb and is characterized by strong kink, moderate red/blue ratio, and a moderate reflectance (20%). This is the only soil that shows a significant 800 to 1000 nm spectral structure, with a weak band centered near 930 nm. The disturbed soil unit was created primarily by rover movement and, in some cases, by airbag retraction. This unit exhibits 22 to 25% peak reflectance, and kink and red/blue ratio values intermediate to those of dark soil and Lamb-like soil. When disturbed, most soils tend to become darker, although their spectral shape does not change. This is probably an effect of the compaction of the soil changing the photometric scattering properties of the uppermost loose surface material.

None of the soils yet analyzed at the landing site show unique evidence for the types of crystalline hematite and/or pyroxene absorption features detected by remote sensing observations of other places on the martian surface (*27, 28*). The origin of the 930-nm absorption seen most prominently in the Lamb-like soil may be an iron oxyhydroxide phase, a magnetic iron oxide, or

a mixture of low Ca pyroxene and iron oxide (*25, 29*). Soils containing iron oxyhydroxide, if verified, provide additional support for past warmer, wetter regimes on Mars.

Rock mineralogy at the Pathfinder Site. There are at least three spectrally distinct rock (and rock-like) materials at the Pathfinder site. The first and most common rock type is called dark rock. The type locations are the upper surfaces of Barnacle Bill and Bamm-Bamm (Fig. 4). Dark rock is characterized by low-contrast spectra with reflectances at 750 nm in the 12 to 14% range. The red/blue ratio is very low, indicating relatively unweathered material, and there is a pronounced decrease in spectral slope in the near-IR beyond 750 nm. For comparison a laboratory spectrum of fresh basalt is shown in Fig. 4 (*26*). Morphologically, members of this type tend to be the intermediate-sized cobbles and small boulders in the scene. They also are more likely to show vugs or vesicles and to have an angular or broken appearance. This is consistent with an origin as ejecta from Big Crater about 2.2 km to the south. None of the rock types exhibit the broad, well-defined absorption bands in the 900- to 1000-nm region that would be indicative of pyroxene (*30*).

Bright rock is the second major type and its type localities are the Broken Wall and Wedge. These rocks are brighter (19 to 24% reflectance) and have higher red/blue ratios than dark rock, indicating more weathering or greater contamination by dust coatings. Some individual rocks in this unit show a decreased slope in the near-IR and some are flat in that region. Most of the larger boulder-sized rocks are members of this spectral unit. This is particularly true of the "Bookshelf" area containing rocks Shark and Half
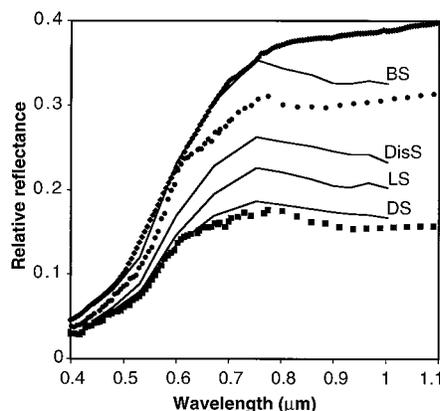

Fig. 3. Relative reflectance spectra of Pathfinder soil types. These spectra include bright soil (BS), disturbed soil (DisS), Lamb-like soil (LS), and dark soil (DS). For comparison the spectra of Mars bright (filled circles), and dark (filled squares) regions and a Hawaiian palagonitic soil (filled diamonds) are included.
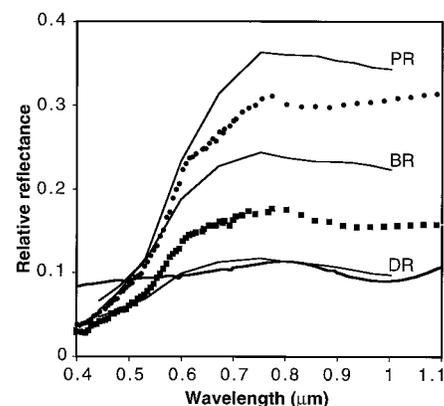

Fig. 4. Relative reflectance spectra of Pathfinder rock types. These spectra include pink rock (PR), bright rock (BR), and dark rock (DR). For comparison the spectra of Mars bright (filled circles) and dark (filled squares) regions and a fresh Hawaiian basalt (heavy line) are included.

Dome, which exhibit a stacked and tilted morphology commonly seen in catastrophic flood deposits. The spectra of these rocks and their α-proton–x-ray spectrometer (APXS) data (*31*) are consistent with the rocks being andesites, but their degree of weathering and mode of deposition indicate that they have been exposed to the surface weathering environment for longer than the dark rock unit.

The last type is called the pink rock for its relatively high blue and red reflectances and large red/blue ratio. The type locations are Scooby Doo and Baker's Bench, but similar material is observed as crusts on rocks, what appears to be crusts in soil, and in areas exposed by the action of rover wheels. The rocks of this type are typically not lying on the surface but appear to be almost completely (Scooby Doo) or partially buried (Casper). The morphology of this unit is consistent with a chemically bonded crust or hardpan, similar to that reported at the VL-2 site (*32*). Digging tests with the rover wheels failed to dislodge any material from Scooby Doo, indicating at least a partially cemented or highly compacted material. The spectra of the pink rock unit are similar to those of bright soil, although brighter in the blue, and APXS measurements of Scooby Doo are also similar to those of bright soil (*31*). This rock type may be a chemically cemented soil whose strongest spectral component is the bright soil.

Dust opacity measurements. About 1300 images of the sun were obtained in the eight low-transmission solar filters through sol 30. We used images taken at 443, 671, 880, and 990 nm to measure and track the
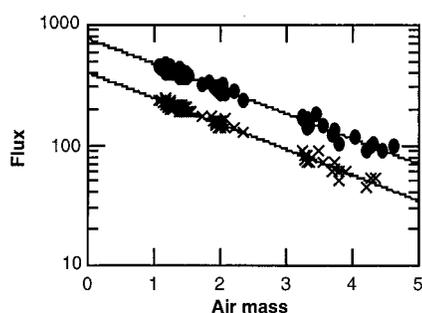
dust opacity as a function of time (*33*). In general, we scheduled images in the four filters once an hour from 7 a.m. to 5 p.m. local solar time (LST) typically at air masses from 1.0 to 5.0 (elevations from 90° to 12° above the horizon). For each image, an air mass is computed from the ephemeris position of the sun and an assumed scale height of 13 km. The resulting flux is then fit as an exponential function of air mass using Beers' law, in which the slope determines the opacity and the intercept is a measure of the solar brightness outside of the atmosphere (Fig. 5). Fitting all intercepts to a model, opacity can be determined for each individual point.

Opacity variations were observed during the day. Afternoon opacity, 0.42 to 0.52, was typically lower than morning opacity, 0.48 to 0.65 (Fig. 6). Afternoon opacities typically increased toward redder wavelengths despite variations of order 0.05 between consecutive sols. Morning opacities exhibited more variation with time and were highest in the blue, occasionally a minimum at 670 nm was observed. The red slope was observed by Viking as was the morning-evening asymmetry (*19*). The preferential increase of blue opacity suggests the formation of a second mode of small particles, which we attribute to water ice (*34*).

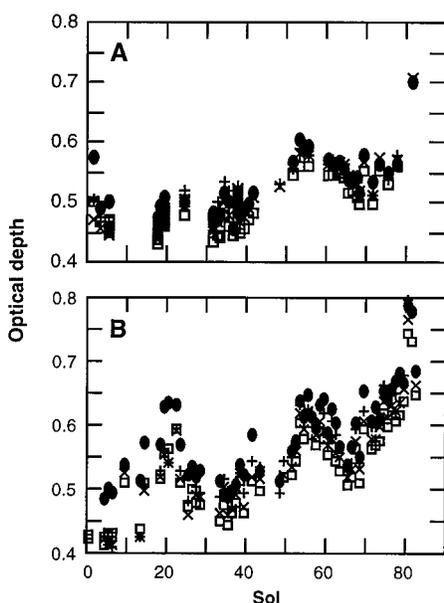The IMP has also been used to determine the optical depth at night by imaging the

zero-magnitude stars Arcturus (α Boo), Vega (α Lyr), and Altair (α Aql). The high optical depth has meant that images through the geology filters typically only provide around 250 counts on these objects in the maximum exposure time of 32.76 s. However, the diopter filter, used to investigate the magnets in the near field, has a much wider bandpass and provides several times the signal at the cost of a smeared image of the star. A reduction of 21 images of Arcturus taken over several nights and an air mass range of 1.0 to 1.7 gives an optical depth of 0.75 ± 0.04. This is higher than the daytime optical depth and probably indicates that water ice has formed on the haze particles.

Aerosol properties. Determining the nature of the aerosol particles in the martian atmosphere is important for understanding the climate in terms of solar energy deposition, thermal opacity, and thus heat balance; to this end, IMP has been used to take sets of images of the sky above the landing site. Each set contains 6 to 13 frames taken at a constant elevation near that of the sun, which was low in the sky (15 to 25° elevation); the 14° wide frames range from 5 or 10° to 180° azimuth from the sun. This allows us to determine almost the entire scattering phase function, under the assumption that the haze is uniform for several hundred kilometers around the landing site. A complete sequence consists of four such sets taken through different filters: 443, 671, 898, and 968 nm; 21 such sequences (10 morning and 11 evening) were returned in the first 30 sols of the Pathfinder mission.

Matching our model to the shape of the forward scattering peak within 20° of the sun (Fig. 7), we can estimate the cross-
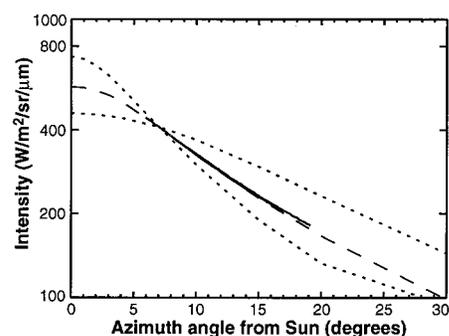
Fig. 5. The variation of flux (w/m²/μm) with air mass (the ratio of the amount of dust along a slant path to that in the direction of the zenith) is shown for 0.45 (circles) and 0.88 (X). The variation seen is not random noise in the measurement, but real variation in the sky. The data shown are limited to the afternoon, when opacity was more stable than in the morning, and are corrected for the varying distance to the sun. The slope of the fits gives an average opacity, while the intercept gives a top of atmosphere value for flux within a filter. Given the top of atmosphere value, an extinction and therefore an opacity can be computed for any datum as $\tau = -\ln(\text{Flux}/\text{Flux0})/\text{air mass}$.

Fig. 6. During the nominal mission, opacity was near 0.5. (**A**) Opacity at noon and later was more stable than the morning opacity (**B**). The wavelengths shown are 0.45 (filled circles), 0.67 (open squares), 0.88 (X), and 0.99 (+) μm. In the morning, opacities were typically higher in the blue and lowest in the red, suggesting a mode of small scatterers, such as water ice clouds, in addition to the 1-μm-sized dust aerosols.

Fig. 7. Sky brightness as a function of azimuth from the sun. A horizontal cut through two images taken on Pathfinder sol 12, converted to real intensity units. The two profiles, one from left of the sun and one from right of it, are overlaid to determine the solar azimuth more precisely. Plotted over the data are three models: The dashed line represents a best fit model, with an effective particle size of 1.0 μm, and a negligible scaling factor. The dotted lines represent models with particle radii too large (2.0 μm, upper peak), and too small (0.5 μm, lower peak).

section weighted, mean particle radius (*35*, *36*). Our estimate for haze particle radius of 1.0 (+0.3,-0.2) μm shows a decrease from the value of 1.85±0.3 μm found by Viking (*37*). This represents the only major difference observed between Pathfinder and Viking with respect to the atmosphere. There is a distribution in sizes around this value and presumably these are the particles that are slowly deposited on the solar arrays and magnetic targets.

Additional information on the haze properties can be obtained by observing the twilight sky. Images of the dawn sky in the direction of sunrise were taken on the mornings of sols 13, 14, 15, 16, 25, and 39. The sol 13 and 14 images were taken in the hour before sunrise; the others included 2 hours before sunrise. On sols 6, 22, and 24 a similar 2 hour sequence was taken of the dusk twilight. The images generally included the horizon at the point of sunrise or sunset as well as additional images at higher elevation angles. At any given time, the brightness of sky was at a maximum about 7° above the local level. The profile of the brightness is interpreted as indicating a bright source function (light multiply scattered through the haze), that increases in brightness toward the horizon, and is opposed by haze extinction that obscures light near the horizon.

The maximum brightness for each wavelength increased exponentially with time. Brightness is compared with the elevation at which the line of sight first intersects the shadow of Mars (*29*). The slope of the exponential fall off is associated with the scale height of the dust and is determined to be 13 ± 1 km. One source of systematic error is the omission of multiple scattering, which must be the dominant source of light 2 hours before sunrise, but this approach is expected to give the approximate scale height. An alternative model is to confine the dust to below 15 km, at which altitude clouds have been observed (*38*). In this case, the mean free path of photons at the top of the dust layer would be about 75 km. At 2 hours before sunrise the terminator is 1700 km away, requiring over 20 scattering events to transport the photons. For dust that extends higher, far fewer scattering events are required, and we consider this situation more likely. Phobos and Deimos illumination of the twilight sky cannot be detected.

While the dawn sky on sols 13 and 14, as well as the dusk sky on sols 6, 22, and 24, had only small-contrast features, the sky was quite varied on other sols. On sol 39 discrete blue clouds were observed from 100 minutes before sunrise until 35 minutes before sunrise. The disappearance of the contrast in the half-hour before sunrise is probably due to changing illumination conditions. For the clouds to be illuminated by direct sunlight at the beginning of the observations, they would have had to be at an altitude of more than 120 km; at the end of the observations they would have to be at an altitude of 25 km. We expect that the clouds are under 120 km and because the illumination of the clouds does not appear to change until after 40 minutes before sunrise, we conclude that the clouds are not directly illuminated. These are water ice clouds, CO_2 condensation is ruled out be-

cause it is expected to occur near 80 km (*34*).

Determination of water vapor abundance. The amount of water expected in the martian atmosphere is only of the order of 10 precipitable micrometers (pr μm) (*40*), sufficient to produce an absorption of about 1.5% in the L4 and R3 filters (935 nm) at an air mass of 10 or more (*1*). To determine the amount of water in the atmosphere of Mars, we observed the disk of the sun in filters L2 (880 nm), R3, and L4 when the sun was high in the sky (elevation angles from 65 to 70°) and the expected absorption in the R3 and L4 filters was much less than 1%. These observations were used to tie the calibration of the three channels together. Next, we observed the sky repeatedly at elevation angles between 3.6 and 6.5° in each of our solar filters. The brightness in all of our filters, including the continuum filter L2, decreased substantially with decreasing elevation angle because of the vertical extinction optical depth of about 0.5. At low elevation angles, the air mass factor depends on the scale height of the dust as well as on the elevation angle observed. A dust scale height of about 13 km was required to give a linear variation of log flux with air mass factor (Fig. 8A).

An error of 1% on the individual L4 and R3 points is attributed to variations in the sensitivity of the detector over the field as the disk of the sun moves across the detector with time (Fig. 8B). The average for the two water bands indicates an absorption of some 1.5%. To convert this absorption to a water abundance, line by line calculations were run using the Air Force Geophysical Laboratory line list in this water band. These data were convolved with the pro-
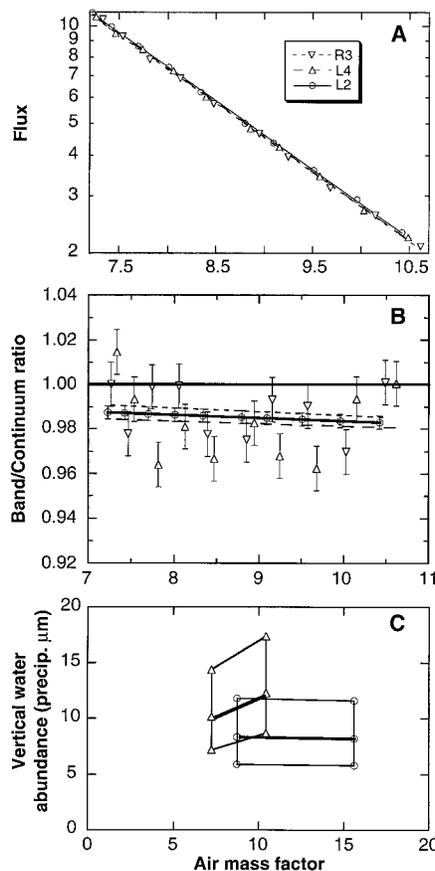

Fig. 8. (**A**) Flux in three solar filters versus air mass factor. The air mass factor was computed for dust distributed with a scale height of 13 km. The exponential fits for the continuum filter L2 and the water band filters L4 and R3 are shown. Note that the water band points tend to lie at lower flux than the continuum filter points. (**B**) The band observations/continuum model for L4 and R3 filters are shown. Linear fits to the band/continuum ratios for the two water-band filters are shown by the short dashes (R3/L2) and long dashes (L4/L2). The average of these two determinations of band/continuum ratio versus air mass is given by the heavy solid line between the dashed lines. (**C**) The vertical water abundance versus air mass factor with the air mass computed assuming the water is distributed with a 13-km scale height (triangles) or with a much smaller vertical scale height (circles).
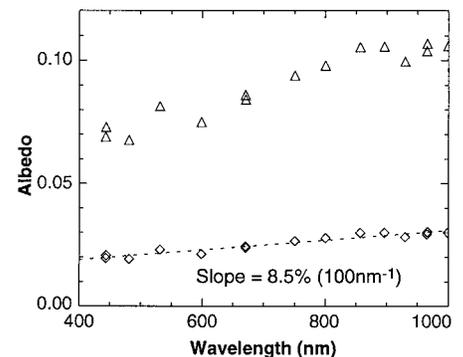

Fig. 9. The observed reflectance of Deimos at a phase angle of 43.4° (diamonds) has been converted into an estimated geometric albedo (triangles) by assuming an optical depth of 0.5 and a phase angle dependence of 0.033 magnitude per degree. The albedo in the range 400 to 650 nm of 0.07 to 0.09 agrees with previous measurements. Note the possible presence of an absorption band at 965 nm.

files of our water filters to construct a curve of growth relevant for martian conditions ($P = 3.5$ mb, $T = 210$ K). This curve of growth indicates a slant water abundance of 45 to 97 pr μm as the sun varied from the greatest to the smallest elevation angle.

This water abundance converts to the abundance in a vertical column by dividing by the appropriate air mass factor (Fig. 8C). The relationship between air mass factor and elevation angle depends on the vertical mixing of the water vapor in the atmosphere. If the water vapor is concentrated at low altitudes by the decreasing temperature with altitude, then the air mass factor can be as large as the inverse of cos (elevation angle). If the scale height is as large as that of the dust, then the air mass factor is some 20% smaller, and the vertical water abundance is correspondingly larger. For small water scale heights, the vertical abundance is 8 (-2, $+4$) pr μm, while for the larger scale height the value is 11 (-4, $+6$) pr μm. Similar analyses for the mornings of sols 15 and 21 and the evening of sol 25 yield 14 ($+7$, -4), 13 ($+7$, -3), and 17 ($+9$, -4) pr μm, respectively.

Astronomical observations. Two spectra of one of Mars' moons, Deimos, were obtained within the first 30 days [Fig. 9, (41)]. A linear least-squares fit to the spectral slope gives a reflectivity gradient of 8.5 per 100 nm; a value not consistent with the much steeper (D-type) slope reported previously (42). Phase curves for Deimos and Phobos have been derived from Viking orbiter images (43). We used these data to produce the geometric albedo within each filter (Fig. 9). A similar set of measurements were obtained at a phase angle of 10.8° and conversion to geometric albedo produced excellent agreement with the result shown in Fig. 9 over the entire wavelength range.

Viking orbiter data were used to derive a geometric albedo of 0.069 ± 0.006 (1σ) in the wavelength range 445 to 593 nm and a rather flat spectrum (43, 44). Our six measurements within this wavelength range give a mean geometric albedo of 0.074 ± 0.006 (1σ), considerably higher than the ground-based results (42). The slope of the spectrum in our data in the range 445 to 593 nm is distorted by the rather high reflectance at 530 nm but may be consistent with Viking observations. However, the increasing reflectance with wavelength to 1000 nm is not consistent with a spectrally flat surface.

There is evidence of an absorption band at 930 nm. This could be caused by an absorbing component in the dust in the martian atmosphere, or by an iron oxide or pyroxene absorption on Deimos. Of these possibilities, the last seems most likely

because of the absence of any major fluctuations in the optical depth of the atmosphere with wavelength. Second, in both spectra, the derived albedo at 530 nm is 10 to 15% higher than expected from a linear increase in reflectance with wavelength. Some phyllosilicates have a generally low and flat albedo with wavelength but an enhanced reflectance in this region of the spectrum.

REFERENCES AND NOTES

1. P. H. Smith and the IMP team, *J. Geophys. Res.* **102**, 4003 (1997). The IMP is multispectral, mineralogical filters from 440 to 1000 nm, and stereoscopic, two eyes separated by 15 cm. The mast, deployed on sol 2, raised the camera 0.61 m to a height of 1.85 m above the martian surface; azimuth and elevation motors allow it to look in any direction (although straight down is a protected, light- and dust-tight position). The resolution is 1 mrad per pixel and the FOV is 14.4°; panoramas are mosaicked from these individual frames.
2. S. F. Hviid *et al.*, *Science* **278**, 1768 (1997).
3. M. Golombek *et al.*, *ibid.* **278**, 1743 (1997).
4. T. A. Mutch *et al.*, *ibid.* **193**, 791 (1976); T. A. Mutch *et al.*, *ibid.* **194**, 87 (1976).
5. Dust is defined as particles less than about 20 μm in diameter and typically is transported in the atmosphere in suspension; sand is comprised of grains 62 to 2000 μm in diameter and is transported typically in saltation (a series of short hops along the surface); granules are defined as particles 2000 to 4000 μm in diameter and are transported by traction along the surface.
6. P. James and J. F. Bell III, personal communication (1997).
7. S. Bagnold, *The Physics of Blown Sand and Desert Dunes* (Methuen, London, 1954); R. Greeley and J. Iversen, *Wind As a Geological Process* (Cambridge Univ. Press, Cambridge, 1984).
8. R. E. Arvidson *et al.*, *Rev. Geophys. Space Phys.* **27**, 39 (1989); R. P. Sharp and M. C. Malin, *Bull. Geol. Soc. Am.* **95**, 1398 (1984).
9. R. Greeley *et al.*, in *Mars* (Univ. of Arizona Press, Tucson, 1992), pp. 730.
10. By matching features in the left and right cameras, an automated machine vision algorithm produces dense range maps of the near field that are projected into a 3-D model as a connected polygonal mesh. Distance and angle measurements can be made on features viewed in the model using a mouse-driven 3-D cursor and a point-and-click interface.
11. J. B. Pollack *et al., J. Atmos. Sci.* **38**, 3 (1981).
12. M. C. Malin, *NASA Tech. Mem.* **4041**, 502 (1988).
13. *Impact and Explosion Cratering*, D. J. Roddy, R. O. Pepin, R. B. Merrill Eds. (Pergammon, New York, 1977), pp. 489–509; *ibid.*, pp. 1043–1056.
14. P. D. Komar, *Sedimentology* **34**, 1165 (1987); P. D. Komar, in *Floods: Hydrological, Sedimentological and Geomorphological Implications*, K. Beven and P. Carling, Eds. (Wiley, New York, 1989), pp. 107–130; P. D. Komar and P. A. Carling, *Sedimentology* **38** (1991).
15. J. E. Costa, *Geol. Soc. Am. Bull.* **94**, 986 (1983).
16. U.S. Geological Survey, Topographic map of the western region of Mars, Atlas of Mars 1:15M Topographic Series, Western Region, Miscellaneous Investigation Map I-2160, Sheet 2 of 3 (1991).
17. G. Komatsu and V. R. Baker, *J. Geophys. Res.* **102**, 4151 (1997).
18. M. C. Malin and D. B. Eppler, *NASA Tech. Mem.* **84211**, 272 (1981); J. E. O'Connor and V. R. Baker, *Geol. Soc. Am. Bull.* **104**, 267 (1992).
19. R. Zurek, *Icarus* **50**, 288 (1982).
20. R. J. Reid, M. S. thesis, University of Arizona (1997).
21. This effect was also observed using Viking Lander imaging data by E. Guinness *et al., J. Geophys. Res.* **92**, E575 (1987).
22. The locations of rock and soil types are shown on the

23. foldout with enlargements of the type localities on the reverse page.
24. The relative reflectance value is a ratio of the measured counts per second for the object in the scene to the counts per second measured for the known reflectance of the IMP radiometric calibration targets when both are subjected to direct solar and diffuse sky illumination. These targets were calibrated in the laboratory relative to Spectralon standards.
25. The red/blue ratio is the ratio of the reflectance of the 600-nm filter divided by the reflectance of the 440-nm filter. The kink parameter, or curvature index, is the deviation between 530 nm and a straight line between the red and blue filters (21).
26. R. Morris, H. V. Lauer Jr., C. A. Lawson, E. K. Gibson Jr., G. A. Nace, C. Stewart, *J. Geophys. Res.* **90**, 3126 (1985); D. M. Sherman, R. G. Burns, V.M. Burns, *ibid.* **87**, 10169 (1982).
27. T. B. McCord, R. L. Huguenin, D. Mink, C. Pieters, *Icarus* **31**, 25 (1977); R. B. Singer, *J. Geophys. Res.* **87**, 10159 (1982).
28. J. F. Bell III, T. B. McCord, P. D. Owensby, *J. Geophys. Res.* **95**, 14447 (1990).
29. J. F. Bell III, in *Mineral Spectroscopy: A Tribute to Roger G. Burns*, Geochemical Society Special Publication 5, M. D. Dyar, C. McCammon, M. W. Schaefer, Eds., pp. 359–380 (1996); S. Murchie *et al.*, *Icarus* **105**, 454 (1993); J. F. Mustard *et al.*, *J. Geophys. Res.* **98**, 3387 (1993).
30. R. Morris, D. C. Golden, J. F. Bell III, H. V. Lauer, Jr., *J. Geophys. Res.* **100**, 5319 (1995); J. L. Bishop, C. M. Pieters, R. G. Burns, *Geochim. Cosmochim. Acta* **57**, 4583 (1993).
31. J. B. Adams, *J. Geophys. Res.* **79**, 4829 (1974); E. A. Cloutis and M. J. Gaffey, *ibid.* **96**, 22809 (1991).
32. R. Rieder *et al.*, *Science* **278**, 1771 (1997).
33. T. A. Mutch *et al.*, *J. Geophys. Res.* **82**, 4452 (1977).
34. Solar images were taken with exposure times of about 1 ms; flight software subtracted a 0-ms image from the original image to correct for the electronic shutter effect, located the sun in the image, and returned a 31 by 31 subframe containing the sun. The dark current (at $-20°C$ in a 1 ms exposure) is typically a small fraction of a count ($< 0.1\%$ of the signal) and is ignored. Flat field uncertainties caused a variation in the integrated flux of ±1%; this was the main source of error. We converted the pixel values from counts to intensity units using the temperature dependent responsivity. The center of the sun is located and a cumulative integral of encircled flux as a function of increasing radius is determined. The background intensity, due to scattered light in the atmosphere and within the camera, is determined and subtracted from the direct sunlight.
35. T. Schofield *et al.*, *Science* **278**, 1752 (1997).
36. The first two frames of each set are taken on either side of the sun, the symmetry of the diffraction is used to determine the solar azimuth more precisely than can be done with only the IMP pointing information (<3 mrad). A pointing uncertainty of ~18 mrad may also exist in elevation, but can be corrected for using the brightness contours in each image. All the pixel counts are calibrated to correct for dark current, flat field, electronic shutter effect, exposure time, and absolute responsivity, yielding intensity values as a function of angle from the sun. We modeled the multiply scattered light using the doubling and adding method. Both spherical (Mie) and nonspherical particles (36) are included in the simulation; their properties in the model may be varied and the output (I/F) is scaled by the solar energy entering the martian atmosphere at each of the filter bandpasses for comparison with the data.
37. J. B. Pollack and J. N. Cuzzi, *J. Atmos. Sci.* **37**, 868 (1980).
38. J. B. Pollack, M. E. Ockert-Bell, M. K. Shepard, *J. Geophys. Res.* **100**, 5235 (1995).
39. T. Clancy, personal communication (1997). This value comes from a study of Hubble Space Telescope images of Mars.
40. R. Kahn, R. Goody, J. B. Pollack, *J. Geophys. Res.* **86**, 5833 (1981).
41. B. Jakosky and R. M. Haberle, in *Mars* (Univ. Arizona Press, Tucson, AZ, 1992), pp. 969–1016.
42. The observations were taken at 16:48 coordinated

Science

Results from the Mars Pathfinder Camera

P. H. Smith, J. F. Bell III, N. T. Bridges, D. T. Britt, L. Gaddis, R. Greeley, H. U. Keller, K. E. Herkenhoff, R. Jaumann, J. R. Johnson, R. L. Kirk, M. Lemmon, J. N. Maki, M. C. Malin, S. L. Murchie, J. Oberst, T. J. Parker, R. J. Reid, R. Sablotny, L. A. Soderblom, C. Stoker, R. Sullivan, N. Thomas, M. G. Tomasko, W. Ward and E. Wegryn

ARTICLE TOOLS	http://science.sciencemag.org/content/278/5344/1758
REFERENCES	This article cites 29 articles, 6 of which you can access for free http://science.sciencemag.org/content/278/5344/1758#BIBL
PERMISSIONS	http://www.sciencemag.org/help/reprints-and-permissions

Use of this article is subject to the Terms of Service